

# Magneto-optical response of graphene: probing substrate interactions

L.A. Chizhova,\* J. Burgdörfer, and F. Libisch  
*Institute for Theoretical Physics, Vienna University of Technology,  
Wiedner Hauptstraße 8-10, 1040 Vienna, Austria, EU*  
(Dated: September 27, 2021)

Magneto-optical transitions between Landau levels can provide precise spectroscopic information on the electronic structure and excitation spectra of graphene, enabling probes of substrate and many-body effects. We calculate the magneto-optical conductivity of large-size graphene flakes using a tight-binding approach. Our method allows us to directly compare the magneto-optical response of an isolated graphene flake with one aligned on hexagonal boron nitride giving rise to a periodic superlattice potential. The substrate interaction induces band gaps away from the Dirac point. In the presence of a perpendicular magnetic field Landau-level like structures emerge from these zero-field band gaps. The energy dependence of these satellite structures is, however, not easily accessible by conventional probes of the density of states by varying the back-gate voltage. Here we propose the magneto-optical probing of the superlattice perturbed spectrum. Our simulation includes magneto-excitonic effects in first-order perturbation theory. Our approach yields a quantitative explanation of recently observed Landau-level dependent renormalizations of the Fermi velocity.

PACS numbers: 73.22.Pr, 71.70.Di, 81.05.ue, 71.70.-d

## I. INTRODUCTION

The progress in fabrication of well-characterized graphene structures led to the availability of graphene devices with mobilities as high as  $6 \cdot 10^5 \text{ cm}^2/\text{Vs}$ <sup>1</sup>. As transport properties are strongly influenced by disorder, the use of suitable substrates such as hexagonal boron nitride (hBN) are key to substantially reduce the amount of substrate-induced bulk disorder compared with conventional SiO<sub>2</sub>, dramatically improving the electronic and transport properties of graphene<sup>2</sup>. These substrates, however, can substantially modify the physical properties of graphene<sup>3,4</sup>. For example, perfectly aligned graphene on hBN features a moiré pattern of 14 nm periodicity due to a small lattice mismatch between the two materials<sup>4</sup>. The superlattice potential leads to the opening of a gap at the Dirac cone and to the folding of the Brillouin zone. Intersections between the original cone and its back-folded replica give rise to additional band gaps energetically above and below the main Dirac cone<sup>4,5</sup>. In the presence of a magnetic field perpendicular to the graphene, secondary satellite Landau levels emanate near these band gaps. Moreover, the large real-space superlattice unit cell allows observing the Hofstadter butterfly<sup>6</sup> at laboratory accessible field strength<sup>7,8</sup>.

Recent experiments<sup>3,7,8</sup> probing the satellite structures and the Hofstadter butterfly of graphene on hBN in a magnetic field have employed a varying back gate voltage ( $V_{\text{bg}}$ ) to control the effective Fermi level  $E_F$  in the graphene sheet. Such a measurement does not, however, provide unambiguous information on the density of states: through quantum capacitance effects and deviations from the idealized linear density of states of graphene (caused, e.g., by the satellite structures), the relation between energy and applied back gate voltage may deviate substantially from expectations<sup>9</sup>. An attractive experimental alternative is magneto-spectroscopy<sup>10-12</sup>.

This technique provides information on the energy difference between the ground state and the particle-hole excitation and, thus, between the different Landau levels. Effective Fermi velocities can be extracted from a fit of Dirac Landau levels to the appropriate transitions. In the presence of a substrate induced moiré potential, the magneto-optical signal can also provide information on the satellites and the evolution of associated Landau levels. The observed shift of the inter-Landau level transitions of graphene on different substrates can be described by a renormalized Fermi velocity and attributed to many-body effects<sup>11,12</sup>. Velocity renormalization was also measured in magneto-Raman scattering experiments<sup>13,14</sup>.

In this work, we determine the magneto-optical conductivity of large ( $140 \times 120 \text{ nm}^2$ ) graphene flakes where the influence of residual edge effects is suppressed by imposing a Berry-Mondragon potential<sup>15</sup> at the boundary (see also Refs.<sup>9,16</sup>). We evaluate the optical conductivity by calculating the dipole transition between the different eigenstates of the flake, which we obtain within the third-nearest neighbor tight-binding approximation. We compare the behavior of a pristine graphene flake with a graphene flake aligned with hBN represented by a superlattice potential<sup>9</sup>. Absorption lines associated with the optical transitions between Landau levels of the Dirac fermions show the expected square root dependence on the magnetic field. For graphene on hBN, we observe a Hofstadter butterfly on top of each transition line. The satellite structures above and below the Dirac cone, which are the signatures of the Brillouin zone folding in graphene aligned with hBN, are shown to contribute to the optical conductivity: our tight-binding approach predicts additional structures in the optical conductivity that evolve linearly with magnetic field, opening a pathway for optical characterization of graphene-substrate interactions. Furthermore, we calculate the shift of the inter-Landau levels transition lines of pris-

tine graphene in the magnetic field due to an attraction of excited electron and hole, i.e. magneto-excitons, on a tight-binding level. We solve a two-body problem and evaluate the direct Coulomb electron-hole interaction within first-order perturbation theory. The resulting velocity renormalization agrees well with the experimental data<sup>11,12</sup> and with complementary theoretical approaches for bulk graphene<sup>17,18</sup>. One advantage of the present tight-binding based approach is the inclusion of spatially varying long-range potentials due to a substrate.

## II. MAGNETO-OPTICAL RESPONSE OF PRISTINE GRAPHENE

The tight-binding (TB) method is very useful for simulating large-scale structures when more sophisticated techniques relying on periodic boundary conditions and small supercell sizes [e.g., density functional theory (DFT)] prove computationally challenging due to the presence of a magnetic field or additional large-scale potential variations. While for small magnetic fields (i.e.  $B \approx 0$ ) the density of states (DOS) [see Fig.1(a)] is dominated by size quantization and properties of the flake boundaries, for increasing field, Landau levels begin to emerge resembling the behavior of bulk graphene. The transition from the linear DOS of bulk graphene at  $B = 0$  to the Landau level regime is governed by the magnetic length  $l_B \simeq 25.5/\sqrt{B[\text{T}]}[\text{nm}]$ . For flakes<sup>16</sup> Landau levels appear when  $l_B$  becomes smaller than the flake diameter  $D$ . The Landau level  $N$  for massless Dirac fermions of graphene satisfies<sup>19</sup>

$$E_N^D = \text{sgn}(N)v_F\sqrt{2e\hbar NB}, \quad (1)$$

which coincides with the high density regions in the calculated DOS [see black dashed curves in Fig.1(a)]. Here  $v_F$  is the Fermi velocity of the Dirac dispersion  $E_D = \pm v_F|\vec{p}|$ . For the present set of tight-binding parameters<sup>20</sup> the Fermi velocity of pristine graphene is  $v_F^0 = 0.78 \cdot 10^6$  m/s. This value of Fermi velocity determined from DFT<sup>21</sup>, however, does not include the many-body effects seen in experiments<sup>22-24</sup> and corrections discussed below.

Landau levels in graphene were observed in transport experiments and were measured by changing the back gate voltage  $V_{\text{bg}}$ . The back gate voltage changes the number of charge carriers  $n = \alpha V_{\text{bg}}$  in graphene and, therefore, the Fermi energy

$$E_F = \hbar v_F \sqrt{\pi n} \quad (2)$$

through capacitive coupling between the back gate and the graphene sheet, where  $\alpha$ , the so-called lever arm, is a measure for the coupling strength. Combining Eqs. (1) and (2) yields straight lines for Landau levels in the  $V_{\text{bg}}$ - $B$  plane in contrast to the square-root behavior in the  $E$ - $B$  plane for Landau levels except of  $N = 0$ . By contrast, magneto-spectroscopy allows for direct probing of

Eq.(1) by optical transitions between Landau levels. Distortions of the linear DOS by traps or localized charge states especially at the device edges, which influence the  $V_{\text{bg}}$  coupling, are largely eliminated.

The selection rule for optically allowed inter-Landau levels transitions is  $\Delta N = |N_f| - |N_i| = \pm 1$ , where  $N_f(N_i)$  is the final (initial) Landau level quantum number<sup>25</sup>. Deviations of the realistic graphene bandstructure from the ideal Dirac cone such as trigonal warping or the perturbation by the interaction with the substrate will break this selection rule, and transitions with  $|\Delta N| > 1$  will become allowed<sup>25</sup>. However, the probability of these transitions remains small. The main transition lines visible in the measured infrared absorption spectra<sup>11,12</sup> are  $T_1 = E_1^D - E_0^D$ ,  $T_2 = E_2^D - E_{-1}^D$  and  $T_3 = E_3^D - E_{-2}^D$ . The analytical forms of the transition energies, which correspond to the peak positions in the associated absorption spectrum, follow from Eq.(1) as

$$\begin{aligned} T_1 &= \sqrt{2|e|\hbar v_F^2 B}, \\ T_2 &= \sqrt{2|e|\hbar v_F^2 B(\sqrt{2} + 1)}, \\ T_3 &= \sqrt{2|e|\hbar v_F^2 B(\sqrt{3} + \sqrt{2})}. \end{aligned} \quad (3)$$

Employing the eigenstates and eigenenergies of the tight-binding calculation for the graphene flake, it is straightforward to obtain the optical dipole transitions between the different eigenstates due to the coupling to the electromagnetic field of the infrared laser. The associated optical conductivity is given in the length gauge by<sup>25</sup>

$$\sigma(\omega) = \frac{ie^2}{\hbar S} \sum \frac{f(\epsilon_a) - f(\epsilon_b)}{\epsilon_a - \epsilon_b - \hbar\omega + i\eta} (\epsilon_a - \epsilon_b) |\langle a|\hat{x}|b\rangle|^2, \quad (4)$$

where  $\omega$  is a photon frequency of the infrared laser,  $S$  is the area of the flake, and  $\epsilon_a$  ( $\epsilon_b$ ) are the eigenenergies of the flake corresponding to the eigenstate  $|a\rangle$  ( $|b\rangle$ ). The summation indices  $a$  and  $b$  extend over all the eigenstates of the flake in the selected energy window. The matrix element  $\langle a|\hat{x}|b\rangle$  gives the transition dipole moment between the two eigenstates. We use the Fermi distribution  $f(\epsilon_{a,b})$  at zero temperature with the chemical potential located at the Dirac point. The difference of Fermi distributions,  $f(\epsilon_a) - f(\epsilon_b)$ , is non-zero for transitions between occupied and unoccupied states corresponding to particle-hole excitation. Zeros in the denominator signify resonant absorption of photons with  $\hbar\omega = \epsilon_a - \epsilon_b$ . In order to avoid numerical instabilities we have introduced a line broadening of  $\eta = 0.1$  meV of the discrete eigenstates of the flake, which is, however, small compared to the physical width of the coarse-grained DOS and, thus, of no consequence for the numerical results.

Real and imaginary parts of the magneto-optical conductivity calculated using Eq.(4) for the pristine graphene flake [Fig.1(b, c)] confirm the dominance of the optically allowed transitions of the Dirac cone also for the finite-size graphene flake. The maxima of the (absorptive) real part of the optical conductivity as well as

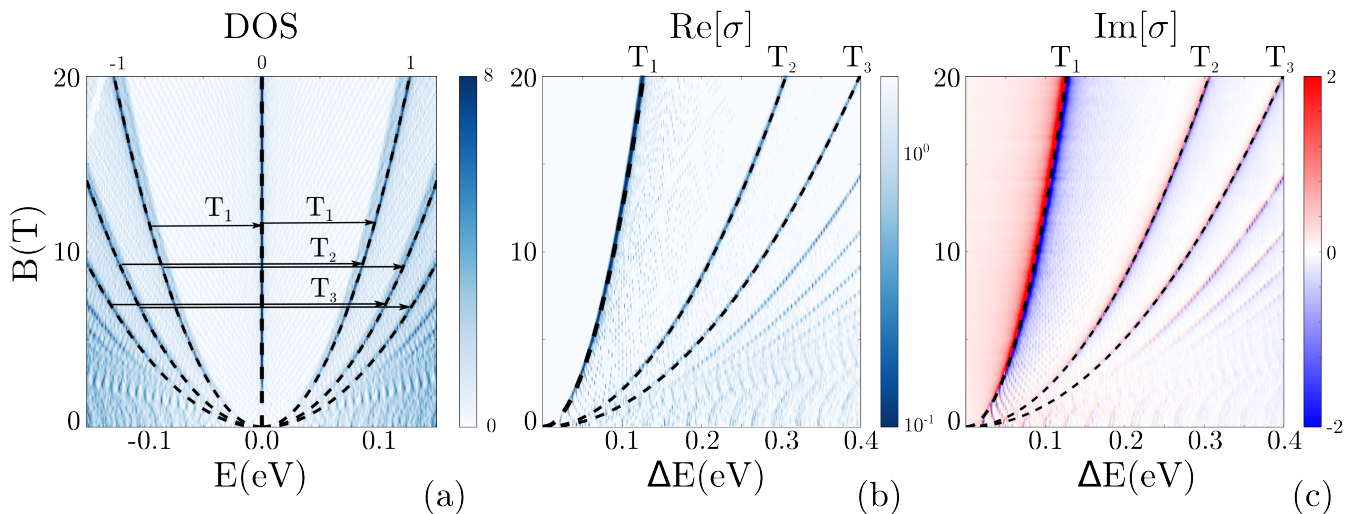


FIG. 1. (a) The density of states of a  $140 \times 120 \text{ nm}^2$  pristine graphene flake as a function of energy and magnetic field. Black dashed curves denote the Landau levels of massless Dirac fermions (Eq.(1)). (b) Real (absorptive) and (c) imaginary (dispersive) part of the optical conductivity  $\sigma$  (color scale) of the flake (evaluated using Eq.(4)) as a function of the excitation energy  $\Delta E = \hbar\omega$  and magnetic field. The black dashed curves are the analytical prediction for the optical inter-Landau levels transitions [see Eq.(3)].

the nodal lines of the (dispersive) imaginary part agree well with the analytical prediction (Eq.(3)) using the Fermi velocity  $v_F^0$  [see black dashed curves in Fig.1(b, c)]. The observed magneto-optical transition lines  $T_1$ ,  $T_2$ ,  $T_3$  etc. are narrow with widths of the Landau levels, of about  $\approx 2 \text{ meV}$  [Fig.1(a)]. Dipole-forbidden transitions with  $\Delta N > 1$  are not visible in Fig.1(b, c) because of their much weaker oscillator strength.

### III. MAGNETO-OPTICAL RESPONSE OF GRAPHENE ON hBN

The tight-binding approximation allows us to study the magneto-optical conductivity of more complex structures with broken periodicity or large periodic supercells. Specifically, perfectly aligned graphene on hexagonal boron nitride (hBN) features a 14 nm periodic moiré pattern due to the small lattice mismatch<sup>4,7,8</sup>. An effective potential reproducing the main features of the measured DOS is of the form<sup>9</sup>

$$V_{\text{BN}}(\vec{r}) = W(\vec{r}) \cdot \sigma_z + V(\vec{r}) \cdot \mathbb{1} + W_{\text{MB}}(B, \vec{r}) \cdot \sigma_z, \quad (5)$$

where  $\sigma_z$  is the Pauli matrix. This potential has the periodicity of the moiré pattern. The first term  $W(\vec{r}) \cdot \sigma_z$  is responsible for the breaking of the sublattice symmetry and for opening of a band gap of  $\Delta = 14 \text{ meV}$  near the Dirac point. The presence of a gap modifies the Dirac Landau levels to

$$E_N^D(B) = \begin{cases} \text{sgn}(N) \sqrt{2|e|\hbar v_F^2 |N|B + (\Delta/2)^2} : N \neq 0 \\ \pm \Delta/2 : N = 0^\pm, \end{cases} \quad (6)$$

The two zeroth Landau levels to which we assign the quantum numbers  $0^+$  and  $0^-$  corresponding to energies  $\pm \Delta/2$  emerge as a result of the valley splitting. The valley degeneracy of the other Landau levels is not lifted. The second term in Eq.(5) is a smoothly varying potential accounting for stronger binding in regions where one sublattice of graphene is on top of boron and another sublattice is in the middle of the BN hexagon. This term accounts for the increased electron-hole asymmetry beyond the third nearest-neighbor tight-binding approximation. In addition,  $V(\vec{r})$  may modify the Fermi velocity. For the parameters of  $V(\vec{r})$  considered, the Fermi velocity of graphene subject to superlattice potential of hBN decreases to  $v_F^{\text{hBN}} = 0.76 \cdot 10^6 \text{ m/s}$ , which is slightly smaller than that of pristine graphene  $v_F^0$ . Finally, the last term  $W_{\text{MB}}(B, \vec{r}) \cdot \sigma_z$  in Eq.(5) describes, on a phenomenological level, magnetic-field dependent many-body effects and accounts for the magnetic-field induced valley splitting. The lifting of the four-fold degenerate (two-fold for valley and two-fold for spin) zeroth Landau level was observed in graphene on  $\text{SiO}_2$ <sup>26,27</sup>, hBN<sup>8,28</sup> and in suspended graphene<sup>29</sup>. In graphene on hBN<sup>28</sup>, the valley splitting was experimentally found to be linearly proportional to the magnetic field, a result which is still unexplained by theory. Two alternative theoretical methods have been previously proposed to explain this observation. (i) One model, based on the continuous Dirac model in the Hartree-Fock approximation, predicts a  $\sqrt{B}$  scaling of the valley splitting<sup>30,31</sup>. While this scaling differs from the linear scaling, the resulting numerical values for the valley splitting resembles those of the experiment within the range of investigated magnetic field strength. (ii) The second model, based on the effect of lattice distortion and the inter-

action with the substrate, predicts linear scaling of valley splitting with  $B$  but underestimates the strength of the splitting by an order of magnitude<sup>32</sup>. In the present work, we account for the valley splitting within the single-electron model by applying the phenomenological potential  $W_{\text{MB}}(B, \vec{r})$ , which depends linearly on the magnetic field with the spatially averaged value  $\bar{W}_{\text{MB}}(B) = 8B[\text{T}]$  meV/T consistent with experiment<sup>28</sup>. The spatial variation of the potential  $W_{\text{MB}}$  follows the Gaussian shape of  $V(\vec{r})$ , i.e.  $W_{\text{MB}}(B, \vec{r}) = \bar{W}_{\text{MB}}(B) \cdot V(\vec{r}) / \langle V(\vec{r}) \rangle$ . (The Zeeman spin splitting, also proportional to  $B$ , is neglected in the following).

The DOS of the graphene flake on hBN [Fig.2(a)] as well as the optical conductivity [Fig.2(b, c)] feature the square-root scaling for the  $N \neq 0$  Landau levels  $E_N^D \sim \sqrt{B}$  of massive Dirac fermions given by Eq.(6) [see black dashed curves in Fig.2(a)] for magnetic fields up to  $B \approx 10$  T. By contrast, the linear magnetic field dependence of the zeroth Landau level is determined by the effective many-body potential  $W_{\text{MB}}(\vec{r})$ . [If  $W_{\text{MB}} = 0$ , the zeroth Landau levels, i.e.  $0^+$  and  $0^-$ , coincide with the magnetic field independent vertical black dashed curves in Fig.2(a)]. The position of the absorption lines in the calculated optical conductivity agrees with the energy difference between Landau levels (Eq.(6)) for  $N \neq 0$  using Fermi velocity  $v_F^{\text{BN}}$ . For transitions involving the zeroth ( $N = 0$ ) level, e.g. the  $T_1$  transition, we have to include in Eq.(6) the linear magnetic field dependence of the  $0^-$  Landau level [see red dashed curve in Fig.2(b)]. The sensitivity of the  $T_1$  transition to the many-body valley (and spin) splitting in the zeroth Landau level offers an alternative to activation gaps measurements.<sup>28</sup>

At higher magnetic fields, the Hofstadter butterfly<sup>6</sup> becomes visible as "diamond"-like structures on top of each Landau level in the DOS [see Fig.2(a) at  $B \gtrsim 10$  T]. This phenomenon arises due to the competition between two length scales: the magnetic length  $l_B = 25.5/\sqrt{B[\text{T}]}[\text{nm}]$  and the scale of the hBN superlattice with a period of 14 nm. At  $B = 25$  T, i.e. when the magnetic flux through the superlattice unit cell is equal to the magnetic flux quantum, the DOS features the diamonds with the largest extent. The optical conductivity, likewise, features a Hofstadter butterfly modifying the absorption lines [see Fig.2(b, c) at  $B \gtrsim 10$  T]. The energetic width of the diamond (FWHM) of the  $T_1$  transition at 25 T is 20 meV corresponding to the size of the first Landau level diamond obtained from the density of states [Fig.2(a)].

Another superlattice induced effect is the presence of satellites above and below the Dirac point near  $E = -0.15$  eV and  $E = 0.14$  eV at  $B = 0$  [see arrows in Fig.2(a)], which arise due to the avoided crossings between the Dirac cone and its replica. The corresponding Landau levels of the satellites evolve linearly with magnetic field in the DOS. These satellite structures appear also in the optical conductivity as an absorption line starting at  $\Delta E = 0.3$  eV at  $B = 0$  and linearly increasing with  $B$  [marked by arrows in Fig.2(b,c)]. Its slope corresponds to the slope of the satellite Landau

levels. The pronounced difference in the magnetic field evolution of Landau levels of the satellites ( $\sim B$ ) and the main Dirac cone ( $\sim \sqrt{B}$ ) is not obvious when measured as a function of  $V_{\text{bg}}$ . Optical transition spectroscopy appears as an attractive alternative for disentangling Dirac-like and Schrödinger-like dispersions in the bandstructure. Magneto-optical experiments for graphene on hBN<sup>11</sup> have, up to now, not focused on the satellite structures induced by the moiré pattern. While challenging, the experimental observations of the satellites and their magnetic field evolution would yield valuable insight into the influence of the moiré potential on the bandstructure.

#### IV. MAGNETO-EXCITONIC SHIFT OF THE OPTICAL INTER-LANDAU LEVELS ABSORPTION LINES

In the single-particle picture we used so far, the calculated optical conductivity yields the position of absorption lines  $T_i$  in agreement with analytical predictions [Eq.(3)] based on the difference between the corresponding Landau levels of Dirac fermions [Eq.(1) and Eq.(6)] In the experiment<sup>11,12</sup>, however, one observes deviations which can be conveniently parameterized in terms of transition-line dependent Fermi velocities  $v_F^{T_i}$  in the  $\Delta E \sim \sqrt{B}$  relation (Eq.(6)). Their origin are obviously excitonic interactions correcting for particle-hole excitations absent in addition spectroscopy when varying the back-gate potential  $V_{\text{bg}}$ .

The formation of magneto-excitons<sup>18,33</sup> by optical excitations between the Landau levels is a many-body effect. To lowest order the excitonic wave function is a product of an electron and a hole wave function:

$$\Psi_{NM}^{\text{exc}}(\vec{r}_{\text{el}}, \vec{r}_{\text{h}}) = \psi_N(\vec{r}_{\text{el}})\psi_M(\vec{r}_{\text{h}}), \quad (7)$$

where  $\vec{r}_{\text{el}}$  ( $\vec{r}_{\text{h}}$ ) is an electron (hole) coordinate,  $\psi_N$  and  $\psi_M$  correspond to the wave functions of the  $N^{\text{th}}$  and  $M^{\text{th}}$  Landau levels undergoing optical transitions. The corresponding Dirac equation reads

$$\hat{H}\Psi_{NM}^{\text{exc}}(\vec{r}_{\text{el}}, \vec{r}_{\text{h}}) = E\Psi_{NM}^{\text{exc}}(\vec{r}_{\text{el}}, \vec{r}_{\text{h}}), \quad (8)$$

where

$$\hat{H} = \sum_{i=\text{el},\text{h}} v_F \vec{\sigma} \cdot (\vec{p}_i - e\vec{A}) - \frac{e^2}{4\pi\epsilon_0\epsilon |\vec{r}_{\text{el}} - \vec{r}_{\text{h}}|}, \quad (9)$$

$\epsilon$  is a dielectric constant and  $\epsilon_0$  is the permittivity of the vacuum. We use the value of  $\epsilon = 5$  found for graphene on SiO<sub>2</sub> within the random phase approximation (RPA)<sup>34</sup> and also for graphene on hBN<sup>13</sup>. In the absence of the Coulomb interaction [second term in  $\hat{H}$ , Eq.(9)] the excitonic energy coincides with Eq.(3), i.e. the single-particle energy difference. The Coulomb interaction changes the transition energies and leads to the observed energy shift due to particle-hole attraction. Magneto-excitonic effects were studied in detail for the two-dimensional elec-

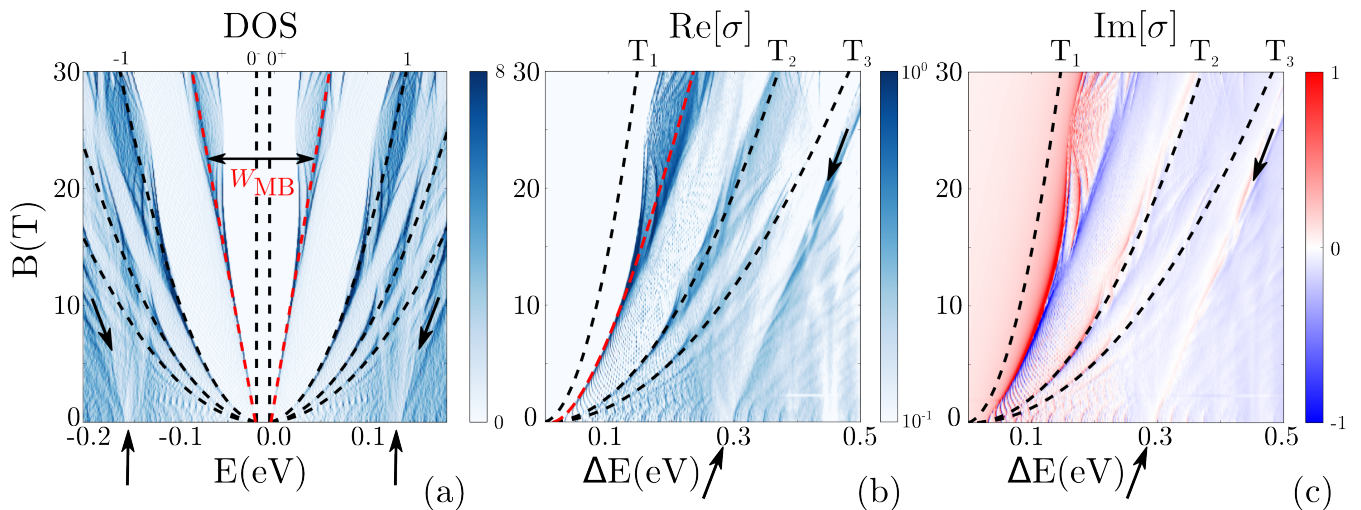


FIG. 2. Same as Fig.1 but for a  $140 \times 120 \text{ nm}^2$  graphene flake deposited on hexagonal boron nitride (hBN) giving rise to a periodic superlattice potential with period 14 nm period. The black dashed curves in (a) correspond to the Landau levels of Dirac fermions with a finite mass [Eq.(6)]. The red dashed lines indicate the magnetic field dependent valley splitting in the zeroth Landau level due to the additional phenomenological potential  $W_{\text{MB}}(B, \vec{r})$ . The satellites above and below the Dirac point at  $B = 0$  and their magnetic field evolution are marked by arrows. In (b) and (c) black dashed curves denote the optical transitions  $T_1$ ,  $T_2$  and  $T_3$ , predicted by the difference between the corresponding Landau levels for massive Dirac fermions (Eq.(6)). The red dashed trace in (b) corresponds to the  $T_1$  transition when the magnetic field dependent valley splitting of the zeroth Landau level is included. The optical transitions between Landau levels at  $B = 0$  of satellites and their B-field evolution are marked by arrows (compare to Fig.1(b,c)).

tron gas<sup>35,36</sup> (2DEG) and for graphene<sup>17,18,33</sup>. In particular, it was shown that the excitation energy consists of several contributions: (i) the (non-interacting) single-particle exciton energy  $\Delta E = E_N^D - E_{N'}^D$  (Eq.(6)); (ii) the direct Coulomb two-particle interaction between the particle and the hole; (iii) the annihilation and creation of electron-hole pairs at different points of the Brillouin zone; and (iv) the exchange interaction. The direct Coulomb term (ii) is negative and gives rise to the excitonic binding. Therefore, the optical transition energy is reduced relative to the estimate in the single-particle picture. Contributions (iii) and (iv) provide positive higher-order corrections, slightly reducing the Coulomb attraction. Since this effect is already, to a certain extent, empirically accounted for by the dielectric response of the medium  $\epsilon$ , we neglect an explicit treatment of these terms.

Within the tight-binding approximation applied to graphene dots, it is possible to treat magneto-excitonic effects. For comparison with the experiment we include the dielectric environment for graphene on a  $\text{SiO}_2$  substrate by taking into account the dielectric constant  $\epsilon = 5$  when evaluating the Coulomb interaction term. We treat the direct Coulomb electron-hole interaction in first-order perturbation theory. Consider an optical transition between the two Landau levels  $N$  and  $M$ . Each of the Landau levels comprises a large number of eigenstates of the flake [see Fig.(1(a))]. A photoexcited state can be written as a superposition of flake eigenstates with energies

in a vicinity of the optically excited Landau levels:

$$\Psi_{NM}^{exc}(\vec{r}_{\text{el}}, \vec{r}_{\text{h}}) = \sum_{a,b} C_{ab} \phi_a^N(\vec{r}_{\text{el}}) \phi_b^M(\vec{r}_{\text{h}}). \quad (10)$$

The expansion coefficients  $C_{ab}$  can be obtained by inserting Eq.(10) into the Dirac equation Eq.(9):

$$(\epsilon_a^N - \epsilon_b^M) C_{ab} - \sum_{a',b'} V_{a'b'}^{ab} C_{a'b'} = \epsilon C_{ab}, \quad (11)$$

with  $\epsilon_a^N$  ( $\epsilon_b^M$ ) being eigenenergies of the flake in the vicinity of  $N^{\text{th}}$  ( $M^{\text{th}}$ ) Landau level. The Coulomb matrix element is

$$V_{a'b'}^{ab} = \frac{e^2}{4\pi\epsilon_0\epsilon} \iint d\vec{r}_{\text{el}} d\vec{r}_{\text{h}} \frac{\phi_{a'}^{*N}(\vec{r}_{\text{el}}) \phi_{b'}^{*M}(\vec{r}_{\text{h}}) \phi_a^N(\vec{r}_{\text{el}}) \phi_b^M(\vec{r}_{\text{h}})}{|\vec{r}_{\text{el}} - \vec{r}_{\text{h}}|} \quad (12)$$

Eq.(11) can be viewed as the Bethe-Salpeter equation (BSE)<sup>37</sup> adapted for a finite-size graphene flake. The Coulomb integral Eq.(12) gives rise to the exciton binding energy. The full solution of Eq.(11) is numerically challenging as the size of the subspace coupled by the Coulomb matrix is given by the product of the number of particle and hole states for each Landau level.

For each Landau level involved in the transition, we consider the energetically closest  $N_S$  eigenstates of the flake. Given the size of our model system, we find that using  $N_S \approx 30-40$  (depending on the magnetic field and

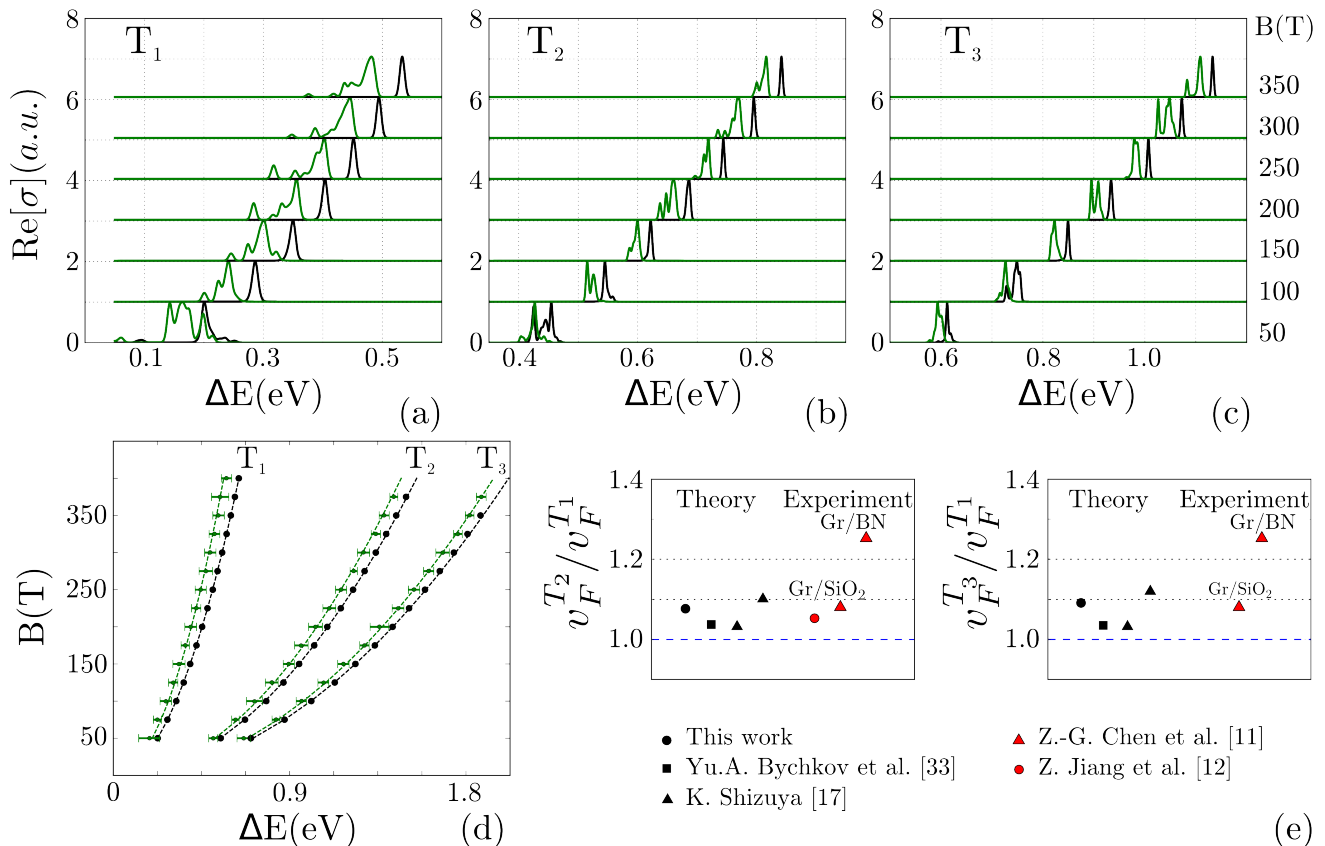


FIG. 3. (a, b, c) Real part of the optical conductivity [renormalized to its maximum] of the transition lines  $T_1$ ,  $T_2$  and  $T_3$  as a function of photon energy. Conductance traces at different magnetic fields are shifted vertically. Black traces correspond to single-particle transitions, green traces correspond to optical transitions taking into account the direct Coulomb electron-hole interactions from first-order perturbation theory. (d) The position (dots) and width (bars) of spectral lines extracted from the first and second moment of the single-particle (black dots) and excitonic excitation spectra (green dots). The black dashed curves correspond to the analytically predicted Landau level transitions given by Eq.(3) with a Fermi velocity  $v_F^0 = 0.78 \cdot 10^6$  m/s. The green dashed curves correspond to the fit of the lines with Eq.(3), however, with renormalized Fermi velocities:  $v_F^{T_1} = 0.69 \cdot 10^6$  m/s,  $v_F^{T_2} = 0.745 \cdot 10^6$  m/s and  $v_F^{T_3} = 0.755 \cdot 10^6$  m/s. (e) The ratio between Fermi velocities of  $T_2$  (right) and  $T_3$  (left) transitions to the Fermi velocity of  $T_1$ : theory versus experiment.

the Landau level index) is a good compromise between accuracy and numerical effort: the matrix dimensions of  $V_{a'b'}^{ab}$  are given by  $N_S^2 \times N_S^2 \approx 10^6$ , were the evaluation of each matrix element requires a double spatial integral with a Coulomb kernel. To keep the problem numerically manageable, we (i) restrict ourselves to first-order perturbation theory<sup>38</sup>, i.e. we include only the diagonal Coulomb matrix elements  $V_{ab}^{ab}$  in Eq.(11) and (ii) reduce the size of the graphene flake to  $24 \times 24$  nm<sup>2</sup>, to speed up the calculation of each matrix element. As we verified numerically, the diagonal elements  $V_{ab}^{ab}$ , indeed, dominate. For each electron-hole pair  $|a, b\rangle$  the corresponding first-order energy correction to the noninteracting electron-hole transition energies  $\epsilon_{a,b}^{(0)} = (\epsilon_a - \epsilon_b)$  is given by the diagonal matrix element

$$\epsilon_{a,b}^{(1)} = V_{ab}^{ab} = \frac{e^2}{4\pi\epsilon_0\epsilon} \iint d\vec{r}_{el} d\vec{r}_h \frac{|\phi_a^N(\vec{r}_{el})|^2 |\phi_b^M(\vec{r}_h)|^2}{|\vec{r}_{el} - \vec{r}_h|}. \quad (13)$$

The binding energy of the  $|a, b\rangle$  exciton is in the diagonal approximation given by  $\epsilon_{a,b} = \epsilon_{a,b}^{(0)} - \epsilon_{a,b}^{(1)}$ .

The optical conductivity of each electron-hole pair, which is related to the dipole matrix element between the electron  $|a\rangle$  and hole  $|b\rangle$  eigenstates, is calculated using Eq.(4), however, now with the excitonic energy contribution included. First-order perturbation theory results in a pronounced shift of the  $T_1$ ,  $T_2$  and  $T_3$  transition lines in the direction of smaller photon energies, when comparing the noninteracting single particle picture [black traces in Fig.3(a,b,c)] with the two-particle correction [green traces in Fig.3(a,b,c)]. The position and the width of the spectral lines is determined by their first and second moments. Neglecting the excitonic effect the transition energies [black dots in Fig.3(d)] agree well with the analytical prediction for inter-Landau levels optical transitions given by Eq.(3) [black curves in Fig.3(d)] with a Fermi velocity  $v_F^0 = 0.78 \cdot 10^6$  m/s determined by our choice of tight-binding parameters for

pristine graphene. In contrast, the two-particle excitonic corrections shift the lines to lower transition energies  $\Delta E$  [green data points in Fig.3(d)]. A fit of these transition lines to the analytic prediction  $\Delta E \sim \sqrt{B}$  yields now line-specific Fermi velocities. In particular, for  $T_1$  the Fermi velocity is  $v_F^{T_1} = 0.69 \cdot 10^6$  m/s; for  $T_2$ ,  $v_F^{T_2} = 0.745 \cdot 10^6$  m/s and for  $T_3$ ,  $v_F^{T_3} = 0.755 \cdot 10^6$  m/s. Such a velocity renormalization, also seen in the experiment<sup>11,12</sup>, clearly reflects excitonic effects. To distinguish effects of the Landau-level specific velocity renormalization from other bandstructure effects that uniformly affect all transitions, we consider the ratio of the renormalized Fermi velocities of  $T_{2,3}$  transitions to that of  $T_1$ . We find reasonable agreement with the experiments<sup>11,12</sup> measuring optical inter-Landau levels transitions for graphene on SiO<sub>2</sub> and also with alternative theoretical approaches for bulk graphene<sup>17,33</sup> [Fig.3(e)]. The present tight binding ansatz allows for including long-range disorder, such as puddles observed in graphene on SiO<sub>2</sub>. We account for the effects of charge puddles by applying a smooth disorder potential with an amplitude of 25 meV (50 meV) and a correlation length of 10 nm (5nm)<sup>39</sup>. Disorder only slightly modifies the theoretically calculated line shifts and velocity renormalization. The resulting optical inter-Landau levels transition lines remain well-defined in the presence of disorder in agreement with magneto-optical experiments for graphene on SiO<sub>2</sub>.

However, the magneto-optical measurements of graphene on hBN<sup>11</sup> notably differ from other measurements and theoretical predictions [see right most point in Fig.3(e)]. This mismatch arises from a substantially ( $\approx 30\%$ ) lower experimental value of  $v_F^{T_1}$  than theoretical predictions and was attributed to many-body effects influencing the zeroth Landau level<sup>11</sup>. Corrections to the dielectric response of the material (i.e., the effective  $\epsilon$ ) should affect all transitions similarly, and thus cannot explain the observed large ratio  $v_F^{T_2}/v_F^{T_1}$ . One effect large enough to explain these findings is the substantial splitting of the four-fold degenerate Landau levels of pristine graphene, as found for graphene on hBN in, e.g., quantum capacitance measurements<sup>7</sup>. However, any such splitting should shift the  $T_1$  line to higher photon energies [as seen in Fig.2(b,c)], i.e. in the opposite direction to that observed in the experiment. Clearly, future magneto-optical experiments for graphene on hBN are

called for to shed more light on this puzzle.

One remark should be added regarding the large values of the magnetic fields used in the simulations to map out Landau levels. Since we consider a flake of a smaller size than in the previous section, the Landau levels emerge at higher magnetic fields. In particular, the Landau level  $N$  is formed as soon as  $2\sqrt{2N}l_B$  is smaller than the smallest dimension of the flake. For example, the  $N = 3$  Landau level participating in the  $T_3$  optical transition becomes distinguishable only at  $B \gtrsim 30$  T for the small flake used to calculate magneto-excitonic corrections. Clearly, the optical response of the larger flakes used in experiment can still be extracted from the present calculation by extrapolating the square root behavior of the optical transitions with transition-dependent Fermi velocity to lower fields.

## V. CONCLUSION

We have simulated the optical properties of graphene flakes with and without moiré potential for aligned graphene on hBN using the tight-binding approximation. Our simulations show that the magneto-optical response allows probing the satellites due to Brillouin zone folding and, unlike probing by back gate voltage, to clearly distinguish energy levels that scale linearly with  $B$  from those that feature a square-root scaling,  $\sim \sqrt{B}$ . We have also shown that excitonic effects can be included in a tight-binding description. We validate our predictions for a Landau-level specific renormalization of the Fermi velocity by comparing to experimental data for graphene on SiO<sub>2</sub>, opening a pathway towards the description of excitonic effects in larger structures. For graphene on hexagonal boron nitride, current experimental data does not fully agree with theoretical predictions, calling for further experimental and theoretical studies.

## ACKNOWLEDGMENTS

We gratefully acknowledge support from the doctoral college Solids4Fun (FWF), as well as by ViCom (SFB 041-ViCom). Calculations were performed on the Vienna Scientific Cluster.

---

\* larisa.chizhova@tuwien.ac.at

<sup>1</sup> N. Tombros, A. Veligura, J. Junesch, J.J. van den Berg, P.J. Zomer, M. Wojtaszek, I.J. Vera Marun, H.T. Jonkman, and B.J. van Wees *J. Appl. Phys.*, **109**, 093702 (2011).

<sup>2</sup> L. Wang, I. Meric, P.Y. Huang, Q. Gao, Y. Gao, H. Tran, T. Taniguchi, K. Watanabe, L.M. Campos, D.A. Muller, J. Guo, P. Kim, J. Hone, K.L. Shepard, and C.R. Dean *Science*, **342**, 614 (2013).

<sup>3</sup> C. R. Dean, A. F. Young, I. Meric, C. Lee, L. Wang, S. Sorgenfrei, K. Watanabe, T. Taniguchi, P. Kim, K. L. Shepard, and J. Hone. *Nature Nano.* **5**, 722 (2010).

<sup>4</sup> Matthew Yankowitz, Jiamin Xue, Daniel Cormode, Javier D. Sanchez-Yamagishi, K. Watanabe, T. Taniguchi, Pablo Jarillo-Herrero, Philippe Jacquod, and Brian J. LeRoy. *Nature Phys.* **8**, 382 (2012).

<sup>5</sup> L.A. Ponomarenko, R.V. Corbachev, G.L. Yu et al. *Nature* **497**, 594 (2014).

<sup>6</sup> Douglas R. Hofstadter. *Phys. Rev. B*, **14**, 2239 (1976).

- <sup>7</sup> G.L. Yu, et al. *Nature Phys.* **10**, 525 (2014).
- <sup>8</sup> B. Hunt, J. D. Sanchez-Yamagishi, A. F. Young, M. Yankowitz, B. J. LeRoy, K. Watanabe, T. Taniguchi, P. Moon, M. Koshino, P. Jarillo-Herrero, and R. C. Ashoori. *Science* **340**, 1427 (2013).
- <sup>9</sup> L.A. Chizhova, F. Libisch, and J. Burgdörfer. *Phys. Rev. B*, **90**, 165404 (2014).
- <sup>10</sup> M.L. Sadowski, G. Martinez, M. Potemski, C. Berger and W.A. de Heer *Phys. Rev. Lett.*, **97**, 266405 (2006).
- <sup>11</sup> Z.-G. Chen, Z. Shi, W. Yang, X. Lu, Y. Lai, H. Yan, F. Wang, G. Zhang, and Z. Li, *Nature Comm.* **5**, 4416 (2014).
- <sup>12</sup> Z. Jiang et.al *Phys. Rev. Lett.* **98**, 197403 (2007).
- <sup>13</sup> C. Faugeras, S. Berciaud, P. Leszczynski, Y. Henni, K. Nogajewski, M. Orlita, T. Taniguchi, K. Watanabe, C. Forsythe, P. Kim, R. Jalil, A.K. Geim, D.M. Basko, and M. Potemski *Phys. Rev. Lett.* **114**, 126804 (2015).
- <sup>14</sup> C. Neumann, S. Reichardt, M. Drögeler, B. Terrés, K. Watanabe, T. Taniguchi, B. Beschoten, S.V. Rotkin, and C. Stampfer. *Nano Lett.* **15**, 1547 (2015)
- <sup>15</sup> M.V. Berry and R.J. Mondragon. *Proc. R. Soc. Lond., Ser. A* **412**, 53 (1987).
- <sup>16</sup> F. Libisch, S. Rotter, J. Güttinger, C. Stampfer, and J. Burgdörfer. *Phys. Rev. B* **81**, 245411 (2010).
- <sup>17</sup> K. Shizuya *Phys. Rev. B* **81**, 075407 (2010)
- <sup>18</sup> A. Iyengar, J. Wang, H.A. Fertig and L. Brey. *Phys. Rev. B* **75**, 125430 (2007).
- <sup>19</sup> I. I. Rabi. *Z. Phys. A* **49**, 507 (1928).
- <sup>20</sup> F. Libisch, S. Rotter, and J. Burgdörfer. *New Jour. of Phys.* , **14**, 123006 (2012).
- <sup>21</sup> S. Reich, J. Maultzsch, C. Thomsen, and P. Ordejón *Phys. Rev. B* **66**, 035412 (2002).
- <sup>22</sup> M. Sprinkle et.al *Phys. Rev. Lett.* **103**, 226803 (2009)
- <sup>23</sup> R. Gillen and J. Robertson *Phys. Rev. B* **82**, 125406 (2010)
- <sup>24</sup> R. S. Deacon, K.C. Chuang, R. J. Nicholas, K. S. Novoselov and A. K. Geim *Phys. Rev. B* **76**, 081406 (2007)
- <sup>25</sup> P. Moon and M. Koshino *Phys. Rev. B* **88**, 241412(R) (2013)
- <sup>26</sup> A. J. M. Giesbers , L.A. Ponomarenko, K.S. Novoselov, A.K. Geim, M.I. Katsnelson, J.C. Maan, and U. Zeitler. *Phys. Rev. B* **80**, 201403(R) (2009).
- <sup>27</sup> Z. Jiang, Y. Zhang, H.L. Stormer, and P. Kim *Phys. Rev. Lett.* **99**, 106802 (2007).
- <sup>28</sup> A. F. Young, C. R. Dean, L. Wang, H. Ren, P. Cadden-Zimansky, K. Watanabe, T. Taniguchi, J. Hone, K. L. Shepard, and P. Kim. *Nature Phys.* **8**, 550 (2012).
- <sup>29</sup> X. Du, I. Skachko, F. Duerr, A. Luican, and E.Y. Andrei *Nature* **462**, 192 (2009).
- <sup>30</sup> D.A. Abanin, B.E. Feldman, A. Yacoby and B.I. Halperin *Phys. Rev. B* **88**, 115407 (2013).
- <sup>31</sup> K. Nomura, and A.H. MacDonald *Phys. Rev. Lett.* **96**, 256602 (2006).
- <sup>32</sup> J.-N. Fuchs and P. Lederer *Phys. Rev. Lett.* **98**, 016803 (2007).
- <sup>33</sup> Yu.A. Bychkov and G. Martinez. *Phys. Rev. B* **77**, 125417 (2008).
- <sup>34</sup> J. Alicea, and M.P.A. Fisher *Phys. Rev. B* **74**, 075422 (2006).
- <sup>35</sup> C. Kallin and B.I. Halperin *Phys. Rev. B* **30**, 5655 (1984)
- <sup>36</sup> H. Haug *Quantum theory of the optical and electronic properties of semiconductors*, World Scientific Publishing Co. Pte. Ltd., 3rd edition (1994).
- <sup>37</sup> L. Yang, M.L. Cohen and S.G. Louie *Phys. Rev. Lett.* **101**, 186401 (2008)
- <sup>38</sup> L.D. Landau and E.M. Lifshitz. *Quantum Mechanics. Non-relativistic theory*, volume 3. Pergamon Press, London, 2nd edition (1965).
- <sup>39</sup> J. Martin et.al *Nature Phys.* **4**, 144 (2007).